J. Fluid Mech. (2014), *vol.* 754, *pp.* 208–231.
doi:10.1017/jfm.2014.388

Roughness-induced turbulent wedges in a hypersonic blunt-body boundary layer

A. Fiala[1], R. Hillier[1,†] and D. Estruch-Samper[1,2]

[1]Department of Aeronautics, Imperial College London, South Kensington, London SW7 2AZ, UK

[2]Department of Mechanical Engineering, National University of Singapore, 117575, Singapore

(Received 2 December 2013; revised 2 June 2014; accepted 30 June 2014; first published online 30 July 2014)

This paper uses measurements of surface heat transfer to study roughness-induced turbulent wedges in a hypersonic boundary layer on a blunt cylinder. A family of wedges was produced by changing the height of an isolated roughness element, providing conditions in the following range: fully effective tripping, for the largest element, with a turbulent wedge forming immediately downstream of the element; a long wake, in length several hundred times the boundary layer thickness, leading ultimately to transition; and retention of laminar flow, for the smallest element. With appropriate element size, a fully intermittent wedge formed, comprising a clear train of turbulent spots.

Key words: compressible boundary layers, high-speed flow, turbulent transition

1. Introduction

Laminar to turbulent transition remains a key subject in high-speed aerodynamics, producing drag and thermal protection problems because of the large increases in skin friction and heat transfer. Early works by Morkovin (1991) and Morkovin, Reshotko & Herbert (1994) summarised the various transition pathways. However, the mechanisms responsible for transition are still poorly understood, and the current ability to predict transitional flows is limited (Reshotko 2008; Schneider 2008; Choudhari *et al.* 2010; Fedorov 2011).

Discrete roughness is a potential issue for high-speed vehicles (e.g. the study of the space shuttle *Endeavour* by Horvath *et al.* 2012). Generally, there will be a minimum scale of roughness, below which the flow downstream of the element remains laminar and eventually becomes indistinguishable from the adjacent boundary layer. The 'critical' size of element is when transition first occurs in the element wake, possibly many hundreds of element heights, or boundary layer thicknesses, downstream. Generally, further increases in the element size cause transition to move closer to the element. The element is 'effective' when further increases in size cause no extra forwards movement of transition, though the associated disturbance field might itself continue to increase (Schneider 2008). The flow around a roughness element is

† Email address for correspondence: r.hillier@imperial.ac.uk

complex, providing a new receptivity environment and a new spectrum of disturbances. For large (effective) roughness elements, absolute instability is likely to dominate (Wheaton *et al.* 2011). However, for small elements, the potential mechanisms are: the growth of instabilities in the element wake, crossflow, Görtler or other transition mechanisms such as the first-mode and second-mode streamwise instabilities described by Mack (1984). The small physical size of elements means that measurement in their immediate vicinity is very difficult, so that most knowledge of their flow field has been generated through computational fluid dynamics (CFD). Although unsteady shedding from bluff bodies is well recognised for low-speed (subsonic) flows, whether uniform or sheared, CFD by Chang & Choudhari (2011) and others show that at supersonic speeds unsteadiness seems to diminish significantly, or vanish, but that large roughness elements (of the order of the boundary layer thickness or larger in height) generate significant upstream separation, with an associated horseshoe vortex wrapped around the element, as well as base-region separation. When elements are smaller in height, the flow is then more characterised by long wakes, hundreds of element heights or boundary layer thicknesses in length, with a clear streak structure along which transitional disturbances can develop (Choudhari *et al.* 2010, 2013; Chang & Choudhari 2011; Wheaton *et al.* 2011; de Tullio & Sandham 2012; de Tullio *et al.* 2013).

The parameter $Re_{\delta_{2,L}}/M_e$ has often been used to interpret transition data (Berry *et al.* 1999; Horvath *et al.* 2000; Thompson 2000; Berry & Hamilton 2002; Reda 2002; Berry & Horvath 2008; Choudhari *et al.* 2013). Berry & Horvath (2008) collate effective transition data from a range of slender blunted bodies to relate the height, k, of diamond-planform roughness elements (as also used here) to the boundary layer thickness, δ, as

$$\frac{Re_{\delta_{2,L}}}{M_e} \approx C_{eff}\left(\frac{k}{\delta}\right)^{-1}, \quad C_{eff} = 70 \pm 14. \tag{1.1}$$

The Reynolds number, based on the roughness height and the flow properties at that height, Re_{kk}, has also been used as a roughness parameter, but with studies under similar conditions finding 'critical' conditions in the broad range $250 \leqslant Re_{kk} \leqslant 900$ (Reda 1979, 2002; Mee 2001, 2002; Schneider 2008). This range is also probably in response to other factors, such as: the considerable difficulty in actually determining critical and effective limits, whether by experiment or CFD; in many experimental studies, the stream disturbance environment and its influence are unknown or not well understood; there is no explicit compressibility dependence; and there may be no distinction between cooled or adiabatic walls. Clearly, element planform shape is important too, and CFD studies by Choudhari *et al.* (2010) suggest that element wake disturbance amplitudes are comparable for diamond- and circular/cylinder-planform elements, but that perturbations generated by spherical elements of the same height are weaker. Experimental data in Berry & Horvath (2008) show that a diamond planform is 'more effective' than single or distributed spheres of the same height. Using direct numerical simulation (DNS), Redford, Sandham & Roberts (2010) introduced a Mach number and wall temperature dependence, relating the critical Re_{kk}, for bump-like elements, to $M_k T_e/T_w$ as

$$\frac{M_k T_e}{T_w} = \frac{3(Re_{kk} - 300)}{700}, \tag{1.2}$$

with Bernardini, Pirozzoli & Orlandi (2012) proposing a modified roughness Reynolds number $Re_k = U_k h/\mu_w$ using the wall viscosity. Equation (1.2) incorporates a more

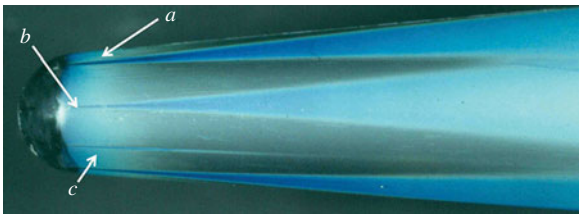

FIGURE 1. Thermochromic liquid crystal image of turbulent wedges on a blunt cone, from Zanchetta (1996).

sensitive parameter dependence, but how such a formulation carries across to the diamond-planform element is not clear.

Many transition studies have considered low- or zero-pressure gradient flows. Nose blunting, however, is an important element of hypersonic vehicle design, and the purpose of the present work is to use measurements of surface heat transfer to explore isolated-roughness-induced transition, and the resultant formation of turbulent wedges, for the blunt-body case. Measurement of transverse profiles through turbulent wedges is rare, especially using multi-sensor arrays with simultaneous sampling so that temporal data can be extracted. Essentially this provides data of practical relevance, it contributes to the development of physical models for turbulent wedges as well as providing potential test cases for CFD modelling.

Physically, nose blunting causes large overall streamwise pressure gradients, and the associated entropy layer, the region of low total pressure and low unit Reynolds number downstream of the curved bow shock wave, enforces a rotational condition at the boundary layer edge. This has a significant impact on transition and a significant complication in the parametrisation of an experiment. Initial blunting of cones, for example, causes a very substantial progressive delay in transition, but when the nose radius Reynolds number, $Re_N = \rho_\infty U_\infty R_N / U_\infty$, is large enough ($\approx$100 000–300 000), early transition – 'transition reversal' – occurs again (e.g. Stetson & Rushton 1967; Softley, Graber & Zempel 1969; Stetson 1988; Schneider 2004). The blunt cone of Zanchetta (1996) (figure 1), tested in the Imperial College tunnel in a 'post-reversal' regime with $Re_N = 1.2 \times 10^6$, shows three different wake structures downstream of discrete roughness elements: (*a*) effective trip; (*b*) transition after a significant wake length; and (*c*) preservation of a laminar wake. This is characteristic of the long wakes referred to above in CFD simulations, except of course that transition has not occurred and that the multiple streaks realised by the CFD cannot be resolved by the experiment. The combination of bluntness and discrete surface roughness is clearly an important regime, but the blunt cone itself is not the most convenient from some perspectives, and a development of the geometry is required, which is described in § 2.2.

2. Experimental details

2.1. *Gun tunnel facility*

The Imperial College gun tunnel operates with nitrogen gas at the nominal conditions given in table 1. The calibration by Mallinson *et al.* (2000) shows weak axial gradients of order $+2.2\,\%\ \mathrm{m}^{-1}$ in Mach number, although this effect is slight over the 334 mm model test length. For data reduction, and laminar CFD, the Prandtl number, Pr, is assumed constant at 0.72, and the viscosity is evaluated using Keyes (1952). The total

M_∞	$\mathrm{d}M/\mathrm{d}x$ (m^{-1})	$P_{0,\infty}$ (MPa)	$T_{0,\infty}$ (K)	T_{wall} (K)	Re_∞ (m^{-1})
8.9 ± 0.05	0.24 ± 0.03	60.8 ± 1.2	1150 ± 45	293 ± 5	47.4×10^6 $\pm 6\,\%$

TABLE 1. Test-section flow conditions at measurement station.

flow duration is 25 ms, with a maximum sample window of established flow of 6 ms at 10 ms from tunnel start.

2.2. *Model design and instrumentation*

The geometry evolved from various basic requirements to provide a generic blunt body for transition studies, and has been used in studies of isolated turbulent spots (Fiala *et al.* 2006) and also shock-induced separation of transitional boundary layers (Estruch-Samper *et al.* 2012). Firstly, we regarded a body of revolution as essential since it avoids the contaminating three-dimensional side effects that are likely with large chord planar bodies. Secondly, multi-sensor heat transfer modules are required, fitted integral with the body surface, to obtain good transverse surface distributions through element wakes. Economical operation requires the same module to be usable over a wide range of chord positions, so that for a body of revolution the test surface must be cylindrical. Thirdly, any blunt body will show a large axial fall in pressure (at Mach $\sim$9 a ratio of order 100:1 from the stagnation point to the cylindrical test surface), so that some management of the distribution is required. The design constraint imposed was that this fall should be monotonic, achieved through iterative CFD design, using a constant-radius, R_B, 'blending arc' between the spherical nose, radius R_N, and the cylindrical measurement surface, diameter D. The latter was set at 75 mm, in part constrained by the tunnel sting system, whilst R_N was set at 25 mm, which provided a nose radius Reynolds number Re_N of 1.2×10^6, the same as the post-reversal state of the blunt cone shown in figure 1. The prime reason for selecting a large nose radius case, however, is that in its downstream development the laminar boundary layer only grows slightly into the adjacent entropy layer. Virtually no 'swallowing' of the entropy layer occurs and the boundary layer edge conditions over the whole test length are very close to body surface conditions inferred from a purely inviscid simulation – the edge Mach number, for example, is everywhere less than 2 % above this inviscid value according to the laminar CFD presented in § 2.3, showing that the boundary layer has barely started to encroach into the entropy layer. The final design is shown in figure 2, with a selected value for R_B of 273 mm. The blending segment maintains continuity in streamwise body slope, but with curvature discontinuities at the two matching points ($x = 17.2$ and 103 mm), which lead to two corresponding pressure gradient changes. This is shown in the CFD of figure 3(*a*), for example, by the predicted surface pressure and the corresponding pressure gradient parameter of Laderman (1980), $(\mathrm{d}p/\mathrm{d}s)\delta_1/\tau_w$, where s is the wetted distance. It should be noted that the axial test section pressure gradient (§ 2.1) is only $\approx$4 % of the bluntness-induced variation along the cylindrical measurement section ($x \geqslant 103$ mm).

The cylinder was constructed from interchangeable segments, allowing measurement of circumferential profiles of heat transfer at four axial locations ($x = 147$, 213, 279 and 347 mm) using a single instrumentation module. This module (see also Fiala *et al.* 2006) comprised 18 thin-film platinum resistance thermometer heat transfer gauges, hand-painted onto a machinable ceramic (MACOR) substrate at 4 mm pitch

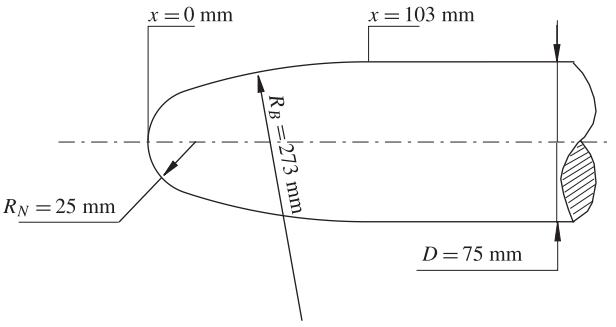

FIGURE 2. Schematic of model nose section.

(6.1°) in azimuth, with spatial resolution of individual sensors of approximately 2.5 mm. The gauge response was such as to register 90 % of a step change in surface heat transfer in 11 μs according to Schultz & Jones (1973). The analogue outputs from the gauges are amplified and low-pass filtered at 45 kHz before being digitised by a 12-bit analogue-to-digital converter at a sample rate of 125 kHz for each channel. The measured surface temperature history was reduced digitally to heat transfer (see Cook & Felderman 1966; Schultz & Jones 1973). The expected error in heat transfer is ±10 %, from a ±5 % uncertainty in the substrate thermal properties, a ±1 % uncertainty in the thin-film thermo-resistive properties, and a ±4 % uncertainty from calibration of the gauges, signal conditioning and spatial resolution. The model surface was maintained in the same highly polished state used for the laminar reference data in figure 4.

2.3. *Reference laminar CFD and experimental data*

The laminar CFD, based on Fiala *et al.* (2006), used a hierarchy of three C-meshes, with successive quadrupling of cell numbers. This gives, for the finest mesh results used here, 696 cells over the streamwise length and at each chordwise station 300 ± 1 cells from the body surface to the shock wave and at least 45 cells through the boundary layer. The difference between predicted surface heat transfer for the 'medium' and 'finest' meshes was everywhere less than 0.5 %; taking account of the uncertainties in free stream conditions in table 1 gives an expected CFD error of ±4 % in surface heat transfer. Figure 3(*b*) shows the entropy layer effect, with the boundary layer edge Mach number and unit Reynolds number substantially less than the free stream values. Because the flow is rotational between the boundary layer edge and the bow shock wave, there was some uncertainty in estimating the boundary layer thickness, δ, from the CFD data. It is taken as the position of 99.5 % recovery of total enthalpy, h_0, from the wall, that is, $h_0 - h_{wall} = 0.995(h_{0,\infty} - h_{wall})$, and the integral thicknesses are evaluated by integration from the wall up to this position. The boundary layer is too thin to quantify these experimentally. The thickness, and integral thicknesses, are estimated to be ±4 % and ±2 % accurate, respectively. Figure 4 presents surface heat transfer measurements together with the laminar CFD prediction, taken from Fiala *et al.* (2006), and table 2 summarises the reference values at various salient locations.

2.4. *Roughness elements*

Each experiment used a single square-planform roughness element, orientated as a 'diamond' configuration, and located at $x_k = 38 \pm 1$ mm (wetted distance from

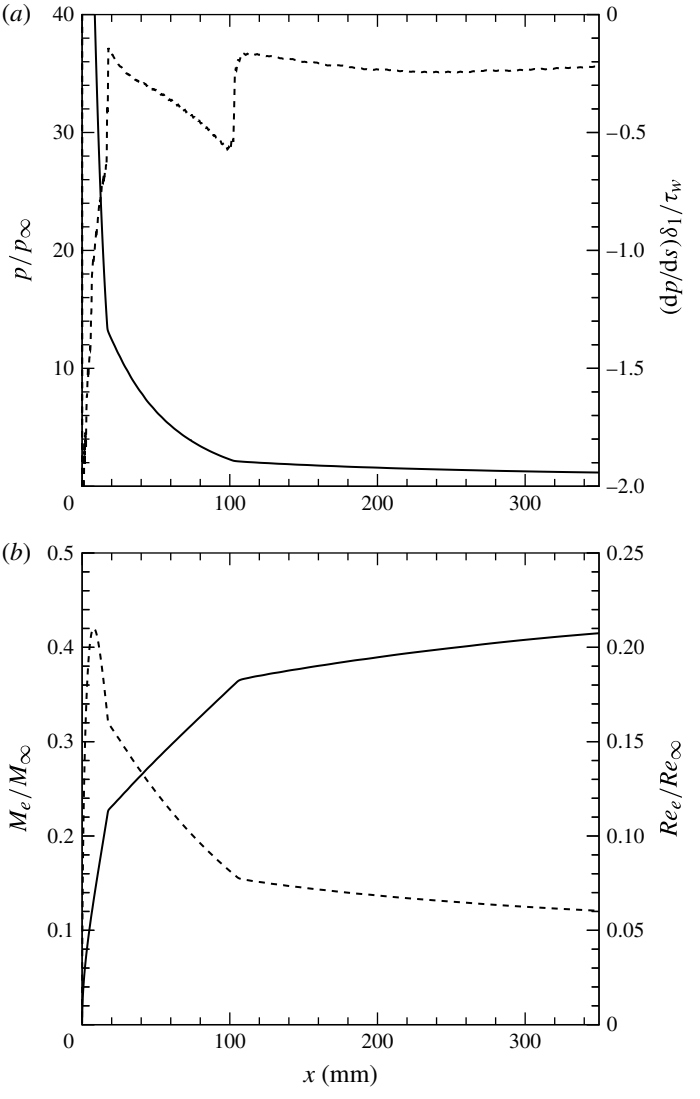

FIGURE 3. Laminar CFD for the variation with axial distance (x) of: (a) surface pressure (solid line) and Laderman parameter for the surface pressure gradient (dashed line); and (b) boundary layer edge Mach number (solid line) and unit Reynolds number (dashed line). The roughness element is located at $x = 38$ mm (also see figure 5); the cylindrical section starts at $x = 103$ mm (see also table 2); the measurement locations are $x = 147$, 213, 279 and 334 mm (see also table 2).

stagnation point $s_k = 53 \pm 1$ mm) as shown in figure 5. This location is on the blending segment, where the boundary layer edge Mach number is supersonic ($M_e \approx 2.3$). The x location was chosen as recognition of the potential sensitivity to small height roughness in the low (supersonic) Mach number, thin boundary layer in the near-nose region. A practical limitation on the forward location of the element was the rapid thinning of the boundary layer, which would make accurate height sizing of the element difficult. The $x_k = 38$ mm location then emerged as a

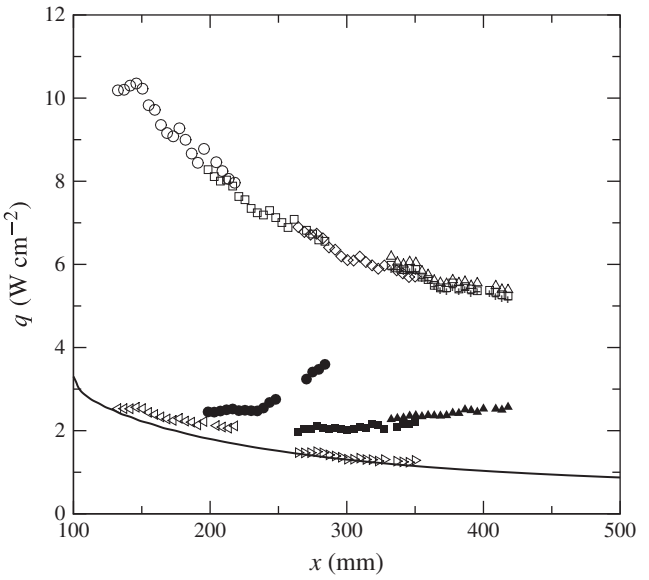

FIGURE 4. Time-averaged surface heat transfer measurements, and laminar CFD (solid line), from Fiala *et al.* (2006). The various symbols represent data from different test runs: ○, □, ◇, △ are for fully roughened nose, with a turbulent boundary layer over the full axial range of measurements; ◁, ▷ are for tests with a highly polished model. Filled symbols: different levels of nose roughening for transitional flow.

x (mm)	M_e	Re_e (m^{-1})	U_e/U_∞	T_e/T_w	δ_x (mm)	$\delta_{1,x}$ (mm)	$\delta_{2,x}$ (mm)	q_L (W cm^{-2})	q_T (W cm^{-2})	Re_{δ_2}/M_e
38	2.30	6.6×10^6	0.74	1.87	0.40	0.08	0.05	11.2	—	156
103	3.17	3.8×10^6	0.84	1.40	1.13	0.29	0.12	2.99	—	144
147	3.30	3.5×10^6	0.85	1.21	1.47	0.44	0.15	2.26	10.3	164
213	3.43	3.3×10^6	0.86	1.14	1.89	0.61	0.20	1.71	8.0	185
279	3.54	3.1×10^6	0.87	1.10	2.28	0.78	0.23	1.38	6.6	202
334	3.61	2.9×10^6	0.88	1.06	2.59	0.92	0.26	1.20	6.0	212

TABLE 2. Reference properties at the roughness element ($x_k = 38$ mm), the blending segment–cylinder junction ($x = 103$ mm) and the four sampling positions ($x = 147$, 213, 279 and 334 mm), evaluated from laminar CFD, apart from the turbulent wall heat transfer rate, q_T, taken from figure 4.

realistic compromise. Five roughness heights (k) were used, with relevant parameters summarised in table 3. This includes the roughness element aspect ratio, width (w_k) divided by height (k), so that the elements have a high aspect ratio and are very 'flat'.

3. Effective trip

The first target was to achieve an effective trip, with early transition and development of a turbulent wedge. Using (1.1), and $Re_{\delta_2,L}/M_e = 156$ from table 2 for the present roughness location, suggests an effective value of $k/\delta \approx 0.45$. At similar

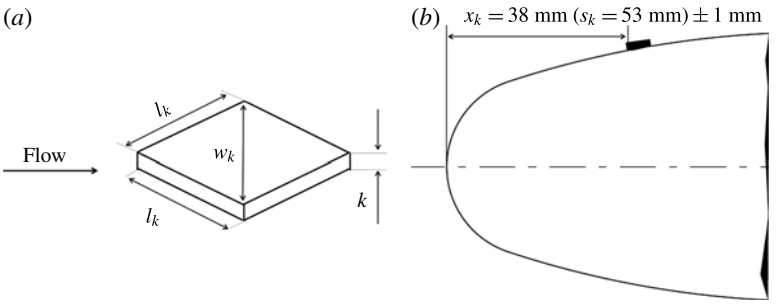

FIGURE 5. Roughness element positioning.

k (mm) ±8 %	k/δ_k ±10 %	$k/\delta_{1,k}$	$k/\delta_{2,k}$	M_k	U_k/U_∞	U_k/U_e	Re_{kk}	Re_{kk}/M_k	w_k (mm)	w_k/k
0.24	0.60	2.96	4.42	2.23	0.70	0.95	1512	679	2.8	11.7
0.12	0.30	1.48	2.21	1.70	0.51	0.70	628	370	2.8, 1.4	23.3, 11.7
0.08	0.20	0.99	1.47	1.32	0.39	0.53	347	263	2.8	35
0.06	0.15	0.74	1.11	1.09	0.31	0.42	227	209	1.4	23.3
0.04	0.10	0.49	0.74	0.81	0.23	0.31	123	152	2.8	70

TABLE 3. Roughness element data: δ_k, $\delta_{1,k}$, and $\delta_{2,k}$ are the undisturbed laminar boundary layer thicknesses at the element location as given in table 2. Here $Re_{kk} = \rho_k U_k k/\mu_k$ is the Reynolds number based on the roughness height k, using undisturbed conditions evaluated at the roughness height; and M_k is the local Mach number at the element height.

values of $Re_{\delta_{2,L}}/M_e$, Berry *et al.* (1999) and Berry *et al.* (1999), Berry & Hamilton (2002) produced early tripping for $k/\delta \approx 0.4$. The Reynolds number, Re_{kk}, for the largest element in table 3 is 1512 and comfortably exceeds the range 250–900 quoted in § 1. For the 'bump' element of Redford, Sandham & Roberts (2012), (1.2) gives a critical value as $k/\delta \approx 0.48$, and it is reasonable to expect that the sharp-edged diamond-planform wedge should have a lower critical value than this. The largest element of the present study, $k/\delta \approx 0.6$ in table 2, exceeds all these various estimates and, as will soon be seen, generated a turbulent wedge with an apparent origin shortly downstream of the element.

Figure 6 presents synchronised time histories, from a single run, for selected gauges in the circumferential array at $x = 279$ mm. The local laminar boundary layer displacement thickness, $\delta_{1,x}$, is used to normalise z and the time normalisation is presented as $-tU_C/\delta_{1,x}$, using the mean convection speed U_C ($= 0.69U_e$) for individual spots in Fiala *et al.* (2006). Heat transfer is presented as measured and also normalised by the predicted (steady) laminar value at the sampling location.

Figure 6 is best considered together with the corresponding space–time contours of figures 7(*c*) and 8. In figure 6 the locations $z/\delta_{1,x}$ of +38.5 and +43.6 show laminar–turbulent fluctuations in the interval $-3200 \leqslant -tU_C/\delta_{1,x} \leqslant -1800$; otherwise the bulk of the signal is fully laminar. Figure 7(*c*) shows that these fluctuations result from the passage of several turbulent spots that are external to, and independent of, the wedge but are close to it and would gradually merge with it further downstream. The disturbances are believed to be triggered by fine particle debris from the rupture of the nozzle throat diaphragm (Estruch-Samper *et al.* 2012). Excluding these external spots,

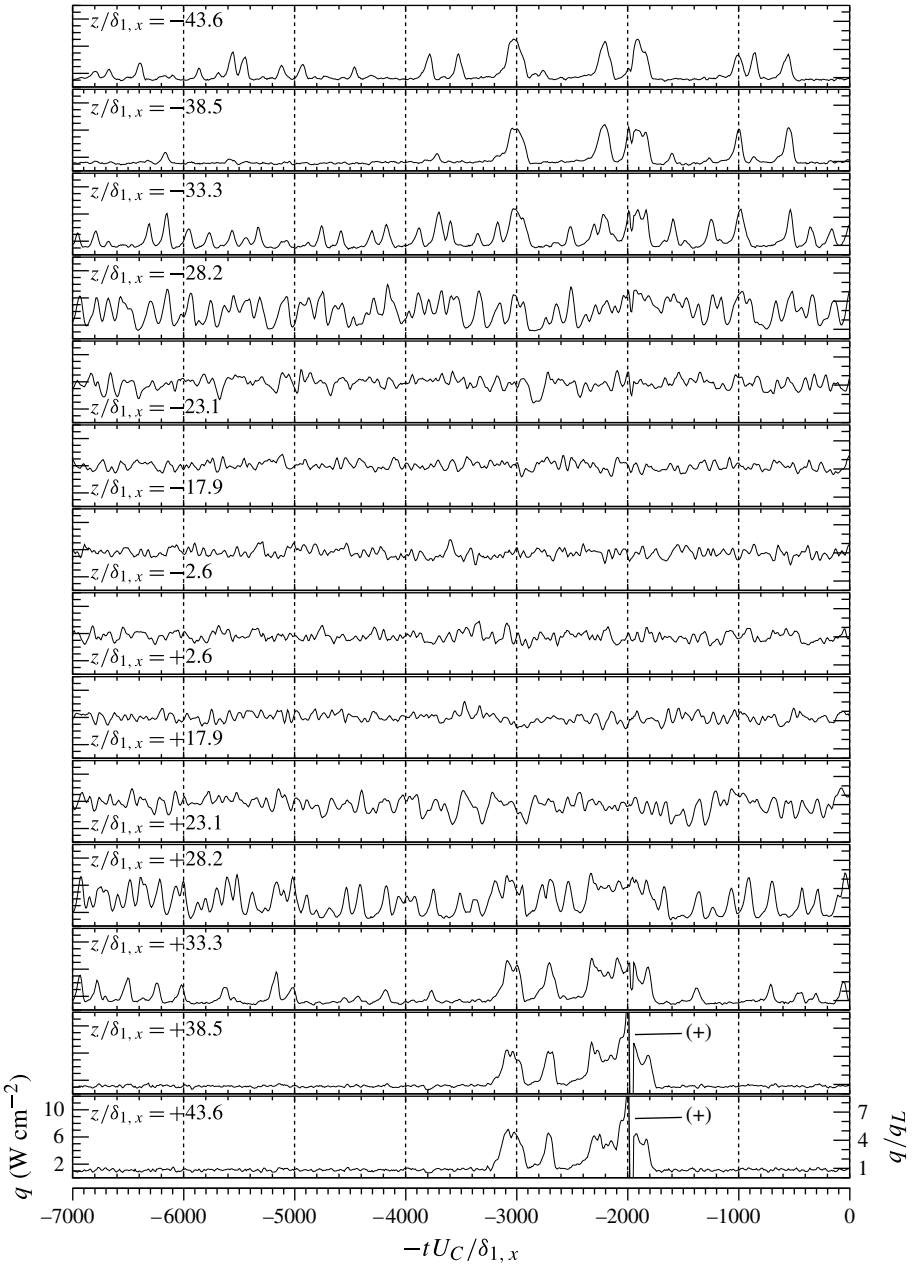

FIGURE 6. Roughness element height $k/\delta_k = 0.60$. Typical time-dependent heat transfer signals, at $x = 279$ mm, for the circumferential array of gauges; $z/\delta_{1,x} = 0$ is the spanwise station immediately downstream of the roughness. The spike detected in some traces at $-tU_C/\delta_{1,x} \approx -2000$ is an electrical pickup from the spark illumination for a schlieren photograph taken during most runs; it has no effect on the fluctuation data.

figures 6 and 7(*c*) suggest that $z/\delta_{1,x} = \pm 28.2$ and ± 33.3 are in an intermittent edge region for the turbulent wedge, with clear excursions between laminar and turbulent values. Further inboard, $z/\delta_{1,x} = \pm 23.1$, shows some large excursions, but never quite

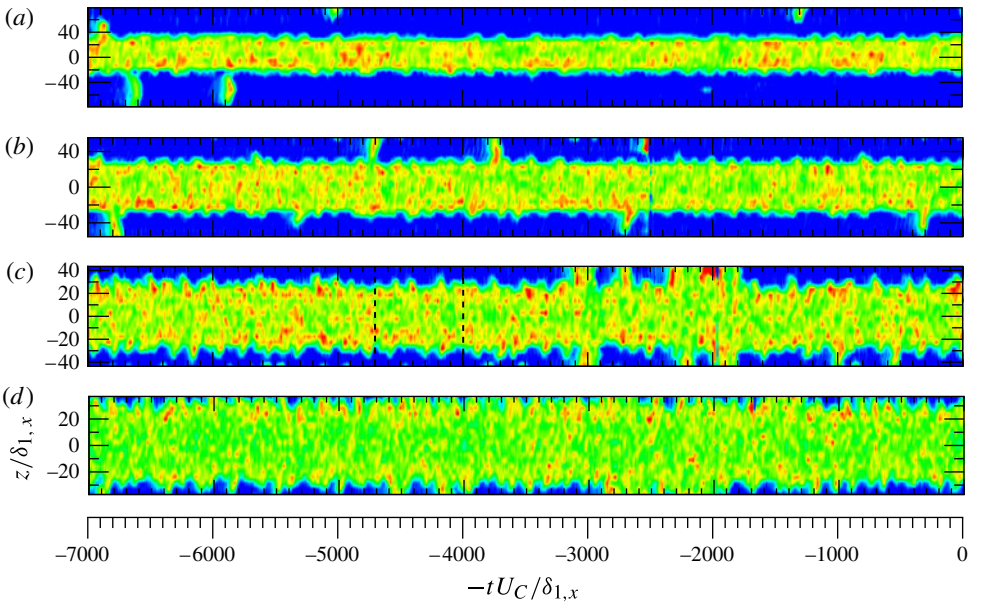

FIGURE 7. Roughness element, $k/\delta_k = 0.60$. Heat transfer contours (blue to red represents low to high heat transfer) in the (t, z) plane at (a) $x = 147$ mm, (b) $x = 213$ mm, (c) $x = 279$ mm and (d) $x = 334$ mm. Panel (c) corresponds to the data of figure 6.

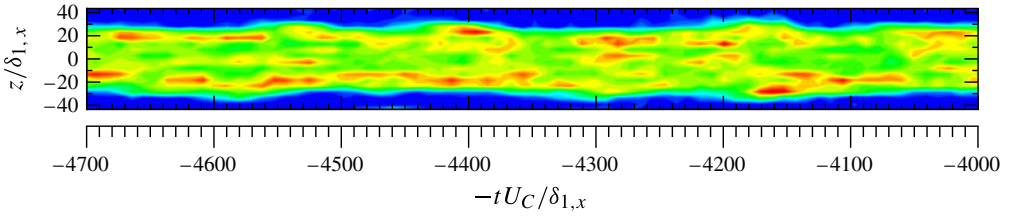

FIGURE 8. Zoom into the region indicated by dashed lines in figure 7(c).

falling to the steady laminar values. Even further inboard, $-17.9 \leqslant z/\delta_{1,x} \leqslant +17.9$, the signal is fully turbulent and is therefore in the turbulent core of the wedge. Figures 7(a,b) and 7(d) show the corresponding contour plots at the other axial sampling locations, clearly showing the spanwise growth of the turbulent wedge with distance.

Figure 9(a,b) presents circumferential distributions of time-averaged heat transfer at the four stations, averaged over two or three repeated runs. The averaging excludes time segments where there are individual spots adjacent to the wedge. All distributions exhibit a slightly concave central profile, with a local maximum near the core boundaries, similar to that reported for some individual spots in Fiala *et al.* (2006). Each distribution undershoots the reference laminar level at the edge of the wedge, though this difference is barely significant compared with the potential combined experimental and CFD errors. Figure 9(b) presents the distributions in normalised form. In physical scale, the turbulent wedge is expected to be very 'flat'; the wedge width of $\approx$50 mm, at the $x = 279$ mm station, for example, is compared with a prediction of $\approx$5 mm for fully turbulent boundary layer thickness, using a simple

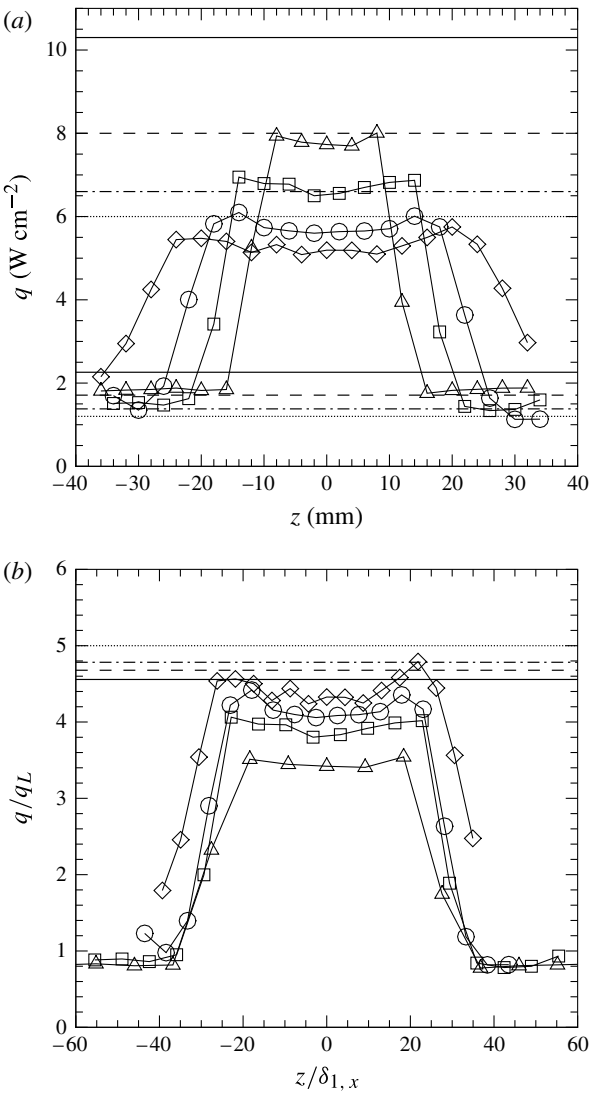

FIGURE 9. (*a*) Roughness element height, $k/\delta_k = 0.60$. Spanwise time-averaged heat transfer distributions at four test locations: △, $x = 147$ mm; □, $x = 213$ mm; ○, $x = 279$ mm; and ◇, $x = 334$ mm. Reference laminar values and turbulent values, from table 2, are shown at each location (solid, $x = 147$ mm; dashed, $x = 213$ mm; dashed-dotted, $x = 279$ mm; dotted, $x = 334$ mm). (*b*) Corresponding data in normalised form, using the local laminar heat transfer and displacement thickness from table 2.

algebraic turbulence model (Baldwin–Lomax) with CFD transition forced at the same position as the location of the roughness element. Flat wedges are also apparent from CFD simulations, such as Choudhari *et al.* (2013) for diamond-planform elements and de Tullio *et al.* (2013) for rectangular elements. This also conforms to the more general observation that lateral spreading rates, controlled essentially by turbulent diffusion and, in particular, destabilisation of the surrounding laminar flow (Gad-el-Haq, Blackwelder & Riley 1981; Redford *et al.* 2012), are significantly larger

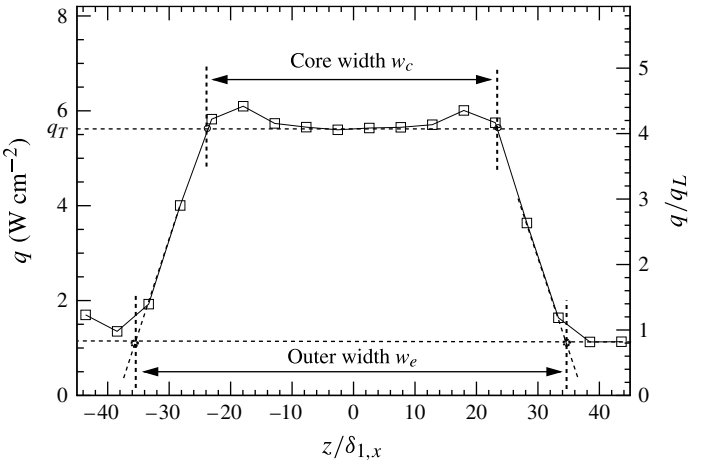

FIGURE 10. Definition of turbulent wedge core and outer boundaries.

than the wall-normal growth rates, which are controlled by turbulent diffusion. Thus, normalisation of spanwise distance by the local laminar boundary layer thickness, in figure 9(*b*), is convenient but not physically meaningful.

Defining the precise lateral extent of the wedge is difficult, through a combination of sensor resolution and interpretation of the data. In essence, the outermost or edge boundary, w_e, is the location where the laminar–turbulent intermittency just falls to zero, and the inner core boundary, w_c, is where the intermittency just rises to 100 %. The sensors do not measure turbulence directly, but it appears from the sensor fluctuations in figure 6 that, as an aid in defining the core boundary, heat transfer excursions to the laminar level disappear in the intervals $-28.2 \leqslant z/\delta_{1,x} \leqslant -23.1$ and $23.1 \leqslant z/\delta_{1,x} \leqslant 28.2$, which are outboard of the local maximum in heat transfer. A similar result was noted for the other measurement stations, with laminar excursions vanishing, for the $x = 334$ mm station, for example, in the intervals $-30.6 \leqslant z/\delta_{1,x} \leqslant -26.2$ and $26.2 \leqslant z/\delta_{1,x} \leqslant 30.6$. Converting these observations to a precise location is not easy, but here we define core width, w_c, as the location, in the region outboard of the local maximum, where the heat transfer has the same value as that in the central core, q_c (i.e. $z \approx 0$). The value q_c was obtained by averaging the two or three central sensor values. All the profiles in figure 9 fall to values slightly below the steady laminar value, and w_e is taken as the interpolated position where q would first reach this measured minimum. These definitions for w_c and w_e are indicated in the schematic of figure 10, using the data for $x = 279$ mm as demonstration, and figure 11 presents their streamwise variation against wetted distance along the surface. The extrapolated wedge origin is a wetted distance, s, of 55 ± 15 mm. Given that wetted distance leads axial distance, x, by 15 mm, this places the projected origin close to the roughness element location of 38 mm. We therefore regard this element as 'effective' and that the near wake of the element is receptive to self-induced wake unsteadiness or external stream disturbances.

For discrete turbulent spots on the same model, Fiala *et al.* (2006) measured maximum width growth rates of $6.75° \pm 1°$, close to the α_e value here. The wedge spreading rates are compared in figure 12 with the data compilation of Fischer (1972*b*), which includes both individual spot and wedge growth rates. The edge spreading rate α_e is the logical basis for comparison, and this lies slightly above

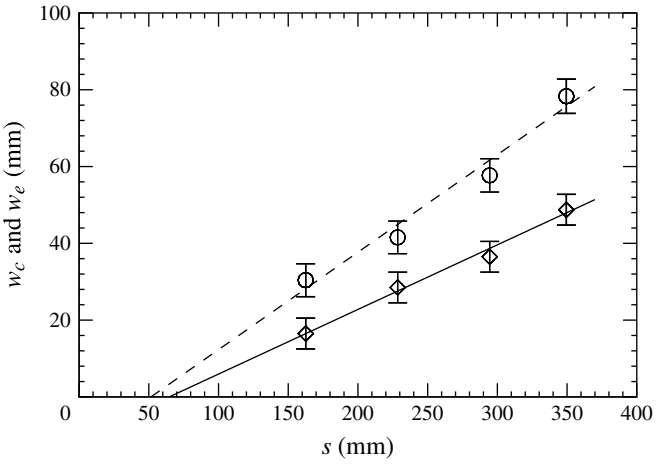

FIGURE 11. Roughness element height, $k/\delta_k = 0.60$. Variation of the wedge core w_c ($\diamond$) and outer w_e (O) widths with wetted distance (s). The least-squares linear fits give wedge core and outer (or edge) spreading half-angles of $\alpha_c = 4.6° \pm 0.9°$ and $\alpha_e = 6.9° \pm 1°$.

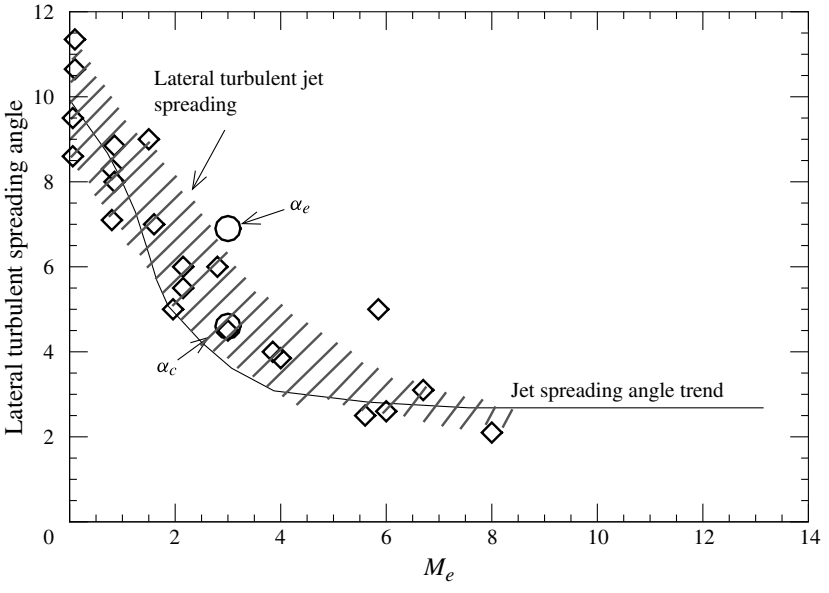

FIGURE 12. Dependence of turbulent spot and wedge lateral spreading rates on edge Mach number, from Fischer (1972*a*). Current measurements (O) for $k/\delta_k = 0.64$ and $M_e \approx 3$.

Fischer's compilation, which was taken from off-surface measurements. Nonetheless, given the uncertainties in determining the actual edge, both in this study and in others, the basic agreement is good. Fischer's data also include a reference to jet spreading rates, a recognition that the lateral spreading rate of wedges is more comparable to that of jets rather than body-normal boundary layer growth. Figure 12 also emphasises that the spreading rate is dependent upon the edge Mach number. In our experiments,

M_e only varies slightly between the four sample stations (see table 2), from $M_e \approx 3.3$ at $x = 147$ mm to $M_e \approx 3.6$ at $x = 334$ mm, but the value at the element location x_k itself is 2.3, so that there is a marked variation along the blending region, where the divergence of the body surface could further accentuate the spreading rate.

Returning to the fluctuation behaviour in the intermittent edge region, figure 6 shows that there are short trains of apparently periodic disturbances, strongly amplitude-modulated, for example at $z/\delta_{1,x} = \pm 28.2$. It should be recognised, nonetheless, that these motions are close to the upper limit of frequency resolution. Section 5 later shows that frequencies characteristic of instabilities developing in the base region, or wake streak structures, are at least an order of magnitude higher than these. The instantaneous distributions in figure 13, for $x = 279$ mm, show the extreme lateral motions achieved over the sample record. Figure 13(*a*) reveals a slight sinuous disturbance of the wedge, essentially preserving the width but with extreme spanwise displacements of the order of ± 7 in $\Delta z/\delta_{1,x}$, and figure 13(*b*) shows limits for varicose motion. The DNS studies in Choudhari *et al.* (2010) and Kegerise *et al.* (2012) on diamond-planform elements in a Mach 3.5 boundary layer, and in de Tullio *et al.* (2013) for square-planform elements at Mach 2.5, both found sinuous and varicose instability modes coexisting in the long streak wake behind the element. However, although such instabilities are likely to be a significant element of the transition process in the present work, especially for the long-wake smaller-height elements studied next, the frequency mismatch referred to above means that the two cannot be linked.

Because of the steep mean transverse gradients in the intermittent regions, the sinuous and varicose disturbances would lead to negative and positive correlation, respectively, for heat transfer fluctuations on opposite outboard sides of the wedge. Figure 14 therefore shows the simultaneous sampling record for gauges at $z/\delta_1 = -28.2$ (q_1) and $+28.2$ (q_2). The second and fourth quadrants correspond to sinuous motions, the first and third to varicose motion. The correlation coefficient between these two locations is -0.12 ± 0.05, that is, a weak predominance of the sinuous motion. The same results are found at the other axial locations.

4. Effects of roughness element height on mean data

The next stage studied systematic reduction of element height. Tests showed that changes of element width w_k were unimportant within our range, illustrated, for example, in figure 15, where the transverse profile is little affected by halving of the element width. Choudhari *et al.* (2010), in simulations for diamond-planform elements, found that the effect on the wake stability of changes in element width were only important once the element aspect ratio fell below approximately 2–3. However, the largest aspect ratios that they considered were less than 5, whereas the minimum studied in the present work (see table 3) is 11.7. It is difficult to comment on the significance of this difference. If the streak patterns identified in the CFD studies, referred to earlier, have their origin in trailing vortex systems shed from the tip, or near-tip, of the diamond elements, then we might conjecture that, whereas for the lower aspect ratios (say ≈ 5) both tip systems clearly are free to interact with each other (as seen in the simulations by the vertical fluid motion on the axis of symmetry), for the larger aspect ratios, the two vortex systems might develop largely independent of each other. If the tip vortex systems are largely independent, for the high-aspect-ratio case, then it might be expected that reductions in this ratio are unlikely to produce significant changes in wake characteristics.

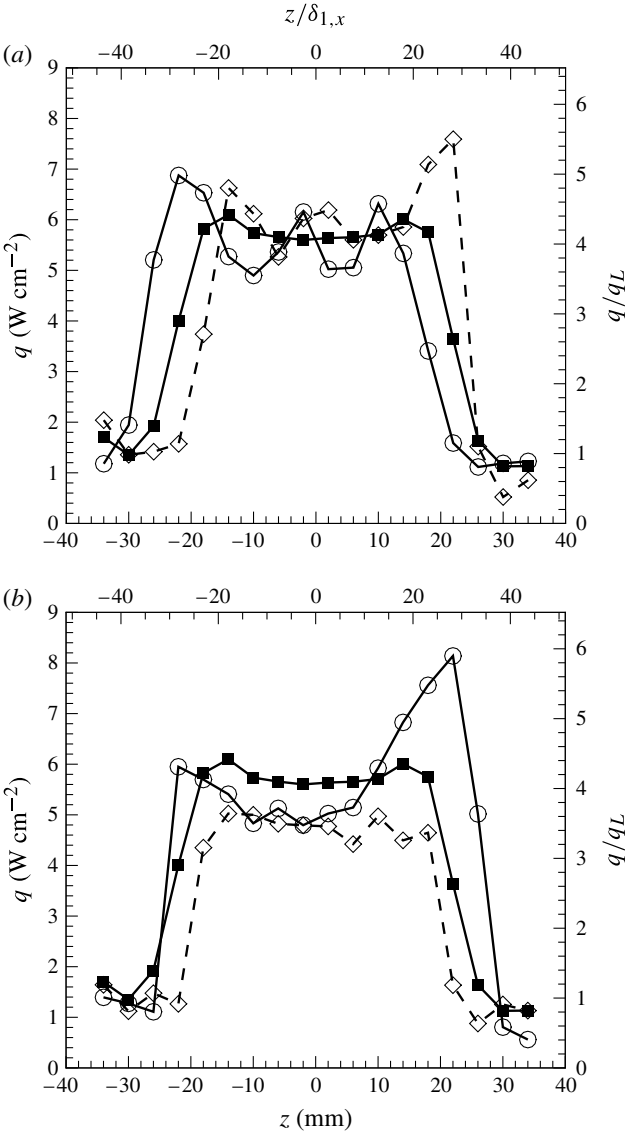

FIGURE 13. Instantaneous heat transfer spanwise distribution for $x = 279$ mm at two different times in each case (open symbols), demonstrating (*a*) lateral 'snaking' of wedge and (*b*) expansion–contraction of the wedge. Solid symbols are the time-averaged values.

Figure 16 presents the time-averaged spanwise heat transfer distributions for the five element heights of table 3. Halving the height from $0.60\delta_k$ to $0.30\delta_k$ reduces the width of the wedge by approximately 10 mm. A similar (7–8 mm) reduction in width is found further upstream at $x = 213$ mm, as shown in figure 17. This implies that both element heights produce virtually the same wedge growth rate, so that the reduction in element height delays the wedge inception point by approximately 80 mm axial distance downstream of the element (i.e. at $x \approx 118$ mm), very close in fact to the second blending position at 103 mm shown in figure 2; the effective trip condition therefore lies between $0.30 < k/\delta_k < 0.60$. With inception at $x \approx 118$ mm,

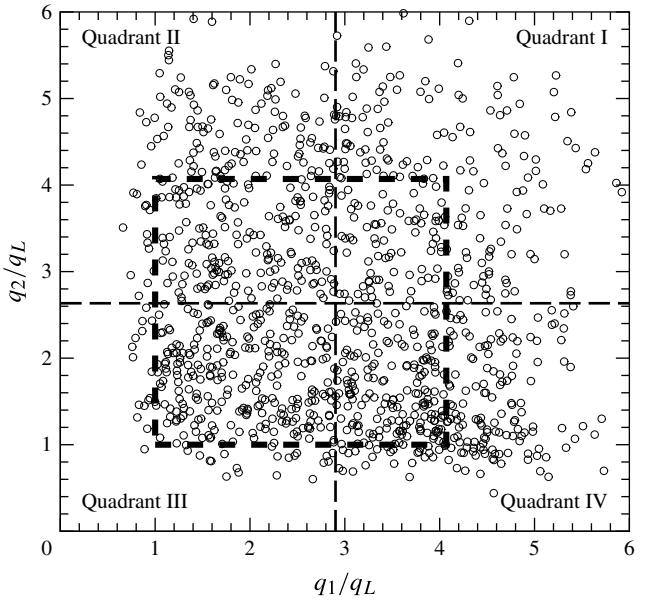

FIGURE 14. Sampling record, at $x = 279$ mm, for gauges located at $z/\delta_1 = -28.2$ (q_1) and $+28.2$ (q_2). Short-dashed thick lines provide the laminar CFD and the core turbulent value q_c as defined in figure 10. The long-dashed lines show the time-averaged data for the two locations.

the element wake has extended at least some 200 boundary layer thicknesses (at the element) before wedge formation, and is likely to experience the streak structures and instability development revealed in simulations such as those in Choudhari *et al.* (2010), Chang & Choudhari (2011), Wheaton *et al.* (2011), de Tullio & Sandham (2012) and de Tullio *et al.* (2013), albeit these are all for zero pressure gradient. The near location of the wedge inception to the blending curve–cylinder junction corresponds to a region characterised by several features. (*a*) The body changes from convex curvature, presumably stabilising, to straight, with δ/R_B changing from 0.001 46 at the roughness element, to 0.0041 just upstream of the junction, to zero downstream of the junction. (*b*) From the element location, to the junction, the body circumference increases by 26 % with presumably a corresponding lateral spreading of streak structures. (*c*) At the same time the boundary layer thickness increases by a factor of 2.8, so that any body-normal enlargement of streak structure dimensions is certain to have an impact upon their lateral scale and spacing as well. (*d*) As noted earlier, there are large reductions in pressure in the streamwise direction, with near-discontinuous changes in gradient at the blending curve–cylinder matching point, the Laderman (1980) pressure gradient parameter, $(\mathrm{d}p/\mathrm{d}s)\delta_1/\tau_w$, in figure 3(*a*), showing a marked reduction in favourable pressure gradient across the matching point from -0.58 to -0.17.

The next reduction in element height to $0.20\delta_k$ produces no significant change in either wedge width or peak heating rates, so presumably also the wedge inception position is unchanged. We assume that, although, almost certainly, streak or trailing vortex disturbances have developed at different rates for the two cases, the reduction in stabilising effect of pressure gradient, or curvature, at the junction is sufficient to 'fix' transition to the junction or shortly downstream. Further reduction to $0.15\delta_k$,

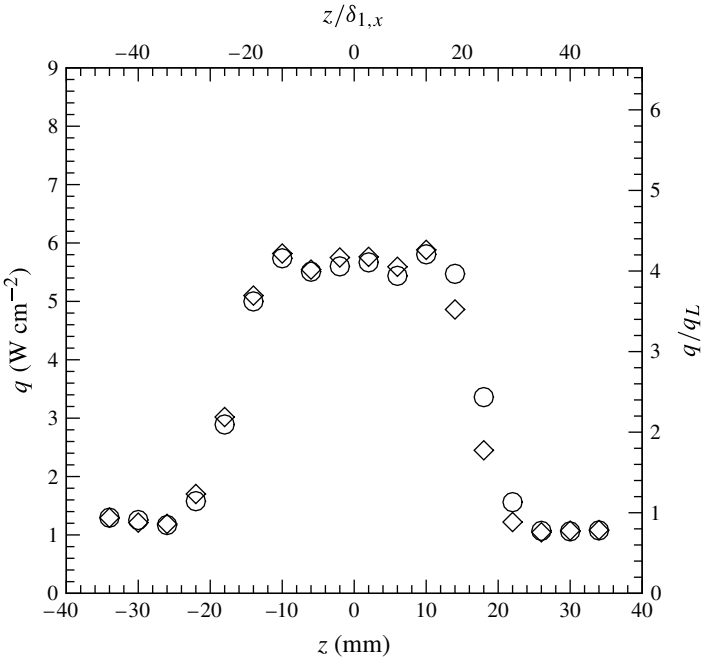

FIGURE 15. Effect of halving element width on the spanwise time-averaged heat transfer distribution, at $x = 279$ mm, for the element height $k/\delta_k = 0.30$: ○, 1.4 mm width ($w_k/k = 11.7$); ◇, 2.8 mm width ($w_k/k = 23.3$).

however, produces a mean heat transfer distribution that everywhere lies between the laminar and core turbulent values, indicating that the wedge is intermittent across its full span with alternating patches of laminar flow and turbulent events. Its width is unchanged, however, suggesting again that the inception location and growth rate are not changed significantly. Final reduction to the smallest height of $0.10\delta_k$ shows that laminar flow is preserved. The incipient element height, taken as the maximum value that still permits a laminar flow downstream of the element, therefore lies between $0.10 < k/\delta_k < 0.15$. Figure 18 summarises the outcome for the various elements. 'Critical' transition conditions take place at the bottom of the previously mentioned range, $Re_{cr,kk} \approx 250$–900 (Reda 1979, 2002; Mee 2001, 2002; Schneider 2008).

5. The intermittent turbulent wedge, $k = 0.15\delta_k$

From figure 16, the centreline value, combined with the laminar and turbulent wedge core heat transfers, implies that the centreline intermittency at $x = 279$ mm is approximately 65 %. Figure 19(*a–f*), for $x = 279$ mm, illustrates different instantaneous states of the intermittent wedge. The panels show a train of turbulent spots, with similar time histories and contour plots in the z–t plane to those found in the isolated spot study of Fiala *et al.* (2006). As seen, the samples are also from test windows where there has been no separate isolated spot formation external to the wedge. The time scale, $-tU_c$, where U_c is a mean convection speed, provides a physical length scale but the contour plot (with one-to-one axis scaling) cannot be regarded as the spot planform shape because the spots do not convect as frozen structures, rather the front (apex) speed, U_f, is about twice the base speed, U_b. Spot studies at hypersonic

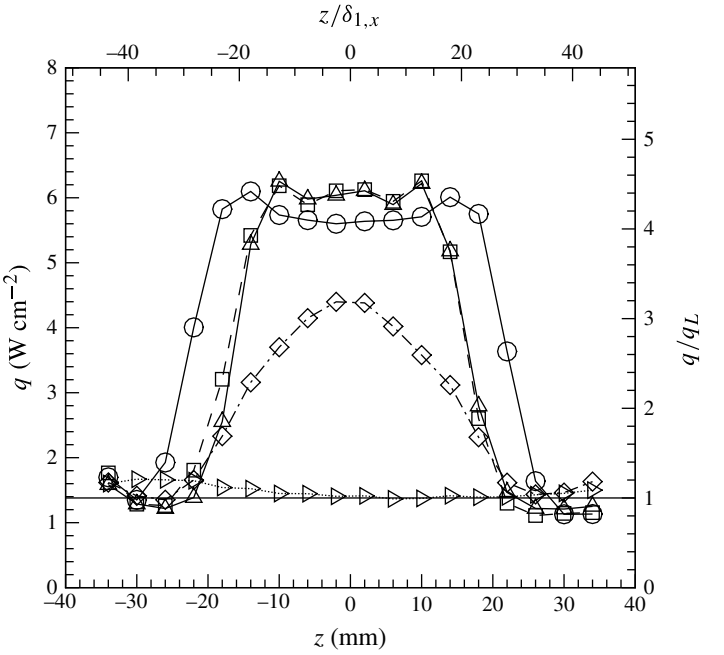

FIGURE 16. Spanwise time-averaged heat transfer distributions, together with the laminar CFD, for all five element heights at $x = 279$ mm: ○, $k/\delta_k = 0.60$; □, $k/\delta_k = 0.30$; △, $k/\delta_k = 0.20$; ◇, $k/\delta_k = 0.15$; ▷, $k/\delta_k = 0.10$. Horizontal line: reference laminar value.

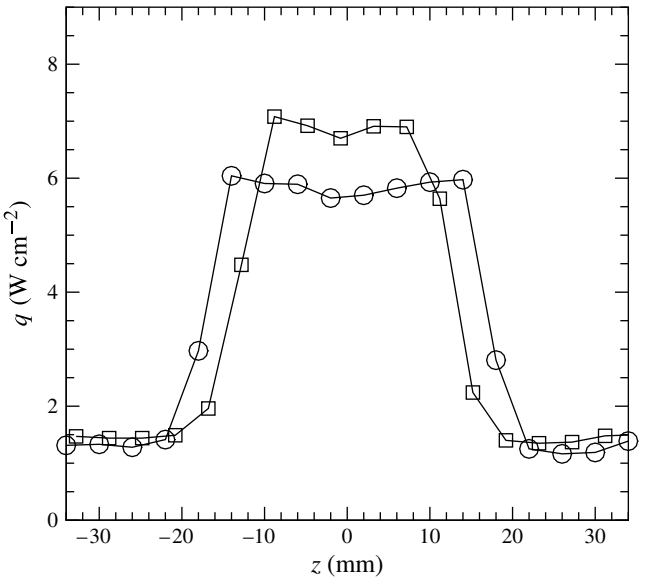

FIGURE 17. Spanwise time-averaged heat transfer distributions at $x = 213$ mm comparing the $k/\delta_k = 0.60$ element (○) with the $k/\delta_k = 0.30$ element (□).

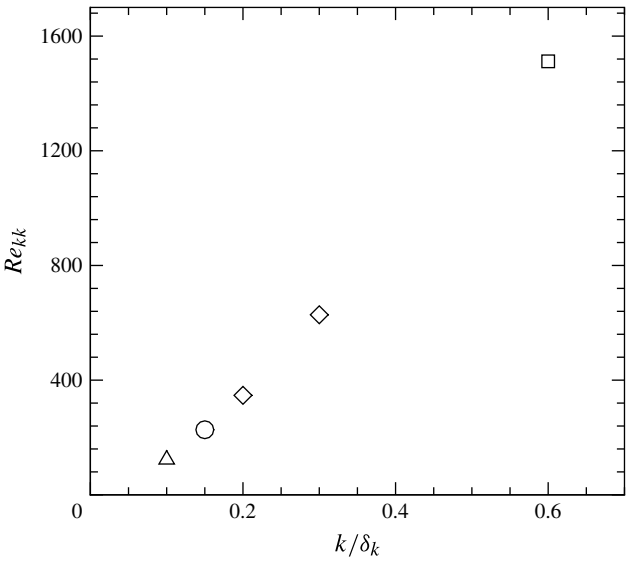

FIGURE 18. Summary of effectiveness of roughness elements, for data taken at $x =$ 279 mm: □, fully effective; ◇, transition in wake of element; ○, train of turbulent spots; △, maintains laminar flow.

speeds are much less extensive than their low-speed counterparts, but surface heat transfer measurements have been used to find convection speeds (e.g. Nagamatsu, Sheer & Graber 1967; Mee & Goyne 1996; Zanchetta & Hillier 1996; Mee 2001, 2002; Fiala *et al.* 2006; Casper, Beresh & Schneider 2011*a*,*b*) and the values used here, $U_b = 0.39U_e$, $U_f = 0.80U_e$, $U_c = 0.69U_e$, are taken from Fiala *et al.* (2006). The same 'flat' structure applies to spots as to wedges referred to in § 3. This is seen, for example, in the simulations of Krishnan & Sandham (2007) and Choudhari *et al.* (2010) for isolated spots and, experimentally, James (1958), Reda (1977, 1979) and Estruch-Samper *et al.* (2012) have visualised the body-normal extent of spots (typically a maximum height less than twice the adjacent laminar boundary layer) and the associated weak wave system generated by the external stream passing over the lower-velocity spot. Spot-induced surface pressure disturbances are correspondingly weak but have been used by Casper *et al.* (2011*a*,*b*) to explore second-mode transition.

Bearing in mind these details of spot structure, some spots, as in figure 19(*a*,*b*), are just starting to amalgamate. In figure 19(*c*,*d*), amalgamation of several spots is well in progress, with the individual structure nearly lost, in this case characterised by a higher frequency for the original individual spots. In contrast, figure 19(*e*,*f*) shows a long calm region between successive turbulent events.

Once spots have formed, the differential convection speeds between fronts and backs means that they will always eventually coalesce with other spots, and so on, to form a fully turbulent wedge – indeed, the 2 : 1 ratio between U_f and U_b means that the spot effectively doubles its length in the time it takes to pass a fixed measurement station. Thus, for a regular production of spots at a fixed location, at frequency f_s (or period $\Delta t_s = 1/f_s$), for the apex of the rearward spot just to catch up with the base of the preceding one at a distance L from inception gives

$$\left(\frac{\Delta t_s U_f}{L}\right)^{-1} = \frac{f_s L}{U_f} \approx \frac{1}{U_f/U_b - 1}. \tag{5.1}$$

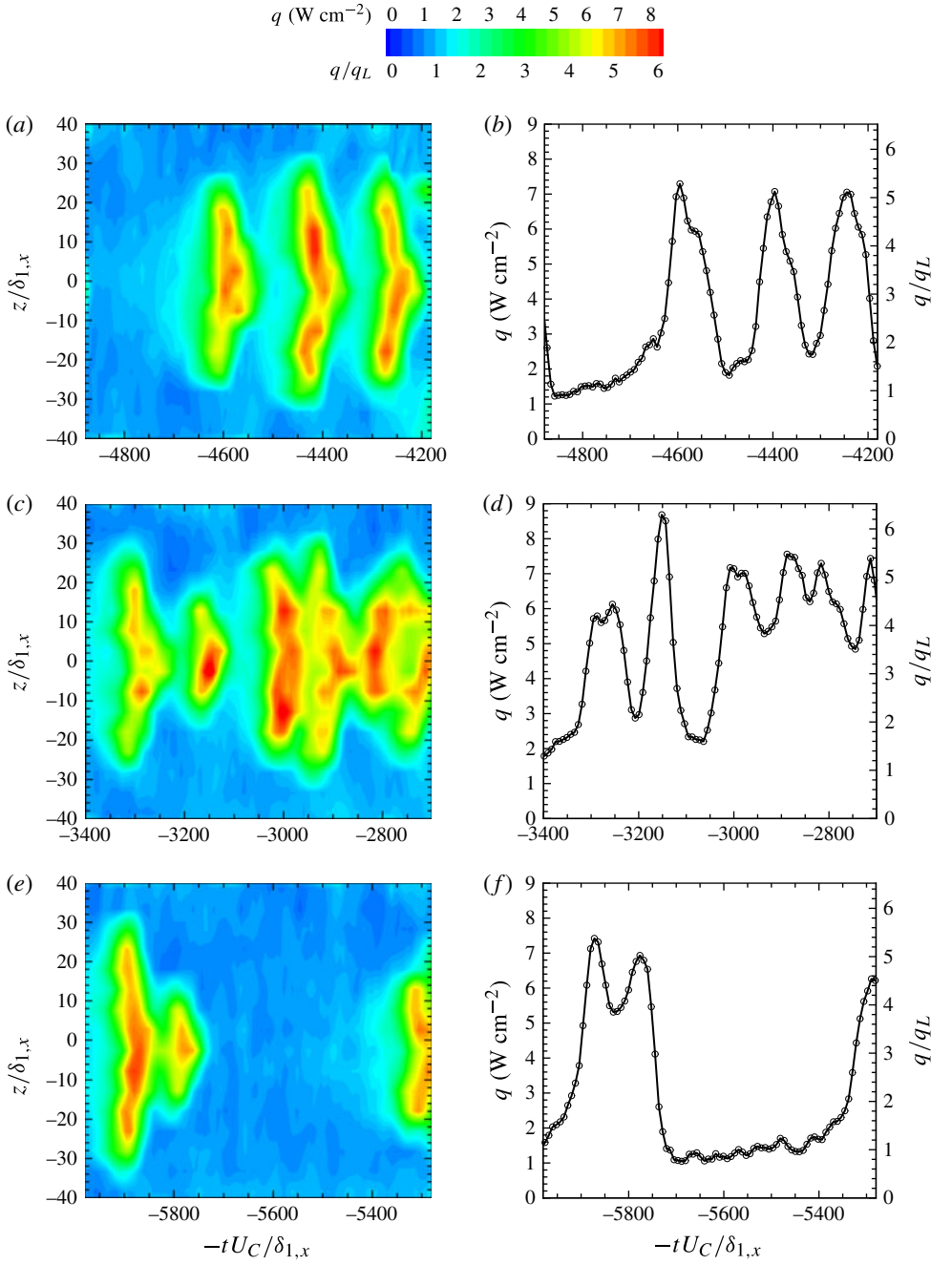

FIGURE 19. Three selected time records for $x = 279$ mm showing heat transfer contours in the (t, z) plane, with the corresponding heat transfer time history near the centreline ($z = -2$ mm, $z/\delta_{1,x} = -2.56$), for element $k = 0.15\delta_k$, $w_k/k = 23.3$.

Using the convection speed values above gives

$$\left(\frac{\Delta t_s U_e}{L}\right)^{-1} = \frac{f_s L}{U_e} \approx 0.77. \tag{5.2}$$

For the train of spots in figure 19(*a*,*b*), just starting to amalgamate, $\Delta t_s U_c/\delta_{1279} \approx 180$. Equation (5.2) then gives $L \approx 182$ mm or, assuming inception at $x = 118$ mm, coalescence by $x \approx 300$ mm, consistent with the actual measurement location of 279 mm. In figure 19(*c*,*d*), the cluster of spots that are already coalescing have a period that is about half the previous, leading to a predicted coalescence location of $x \approx 210$ mm, well upstream of the measurement location. In contrast, the extensive calm region in figure 19(*e*,*f*), of the order of $\Delta t U_c/\delta_{1279} \approx 350$, suggests a chordwise location $x \approx 470$ mm for coalescence to start between the left and right structures in the figure. This suggests that a fully turbulent wedge may not be formed until this distance, nearly 400 times the boundary layer thickness at the blending curve–cylinder junction, and over 1000 times the boundary layer thickness at the roughness element itself. It can also be seen, particularly in figure 19(*c*,*e*), that there is a significant difference in some spanwise scales of spots. The larger spans correspond to the scales expected for inception near the junction, but the smaller spanwise scales correspond to likely inception points well downstream of this.

The $k/\delta_k = 0.15$ element sits between the $k/\delta_k = 0.1$ case, which is repeatably laminar, and the $k/\delta_k = 0.2$ case, which is a repeatably turbulent wedge. One explanation for the behaviour of this intermittent wedge is that it is truly at an 'incipient' condition, where slight alterations in stream conditions or the disturbance environment cause it to switch between receptive and non-receptive states. Thus a turbulent event, or turbulent spot, in figure 19 would not be the development of a single transitional event, but rather the accumulation of a packet of disturbances. This explains why the apparent frequency of the spot trains in figure 19 is significantly lower than the expected frequency for the formation of disturbances at the element and in its wake. As an illustration of the frequencies expected, in figure 19(*a*,*b*) the three structures have a frequency $f\delta_{1279}/U_{e,279} \approx 0.0038$ or $f k/U_k \approx 0.000\,82$ or $f\delta_k/U_{e,k} \approx 0.0023$. Any disturbance source, generated by unsteady shedding directly from the element, is likely to produce values of $f k/U_k = O(0.1)$ to $O(1)$. In a low-speed study, for example, Acarlar & Smith (1987) cite the shedding frequency for hairpin vortices from a hemispherical element $f_s k/U_k$ as ranging from 0.05 to approximately 0.4. Frequencies expected for element wake instability are also high. The work by Choudhari *et al.* (2010) on diamond-element wake-streak instability suggests $f\delta_k/U_{e,k} \approx 0.12$–$0.18$, for sinuous and varicose modes, and values of ≈ 0.14 for the square-planform element in de Tullio *et al.* (2013).

6. Concluding remarks

The bulk of existing studies on individual roughness elements have focused on zero-pressure-gradient boundary layers. The present study relates to a more complex but practical blunt-body flow, distinguished by the thick entropy layer and strong initial favourable pressure gradients, both associated with the blunt nose. Using isolated roughness elements, the effect of changes in element height from 60 % of the boundary layer thickness to 10 % shows a complete sequence from a fully effective trip, with almost immediate formation of a turbulent wedge, through development of a long wake, of order 200 initial boundary layer thicknesses, leading probably to a convective mode of transition, and eventually to preservation of a fully laminar flow. It appears that transition of the long wake is fixed at the blending curve–afterbody junction, or shortly downstream, by various factors, including a significant, abrupt reduction in the favourable pressure gradient. It is difficult to separate out the effects of these various factors, but the body geometry chosen has avoided: the formation

of a pressure undershoot in the axial surface distribution, and the resultant formation of adverse pressure gradient flow; and entropy layer swallowing effects. The element aspect ratio, that is, the span-to-height ratio, is large compared with others used (especially in CFD simulations). Thus, although the large element-wake development lengths, before the onset of transition, are characteristic of simulations of instability development on long streak wakes, it is possible that disturbance development in the present work could also be associated with element tip-vortex systems, which are sufficiently far apart that they might even initially develop independently of each other. In essence, this is a complex flow regime that could be usefully explored by CFD simulations, since achieving sufficiently fine spatial resolution is exceptionally demanding experimentally. It is clear from the smaller elements that substantial lengths of intermittent wedge can be formed, comprising a train of turbulent spots. The most likely explanation for this is that the element wake switches from transition to non-transition, perhaps provoked by fluctuations in stream conditions, and that any given spot is the accumulation of a packet of transitional disturbances. In this case the wake development lengths, before a full turbulent wedge forms, are very large – indeed, potentially even more so if only a slight further reduction in element height were to be made.

REFERENCES

ACARLAR, M. S. & SMITH, C. R. 1987 A study of hairpin vortices in a laminar boundary layer. Part 1. Hairpin vortices generated by a hemisphere protuberance. *J. Fluid Mech.* **175**, 1–41.

BERNARDINI, M., PIROZZOLI, S. & ORLANDI, P. 2012 Compressibility effects on roughness-induced boundary layer transition. *Intl J. Heat Fluid Flow* **35**, 45–51.

BERRY, S. A. & HAMILTON, H. H. 2002 Discrete roughness effects on shuttle Orbiter at Mach 6. *AIAA Paper* 2002-2744.

BERRY, S. A. & HORVATH, T. J. 2008 Discrete-roughness transition for hypersonic flight vehicles. *J. Spacecr. Rockets* **45**, 216–227.

BERRY, S. A., HORVATH, T. J., HOLLIS, B. R., THOMPSON, R. A. & HAMILTON II, H. H. 1999 X-33 hypersonic boundary layer transition. *AIAA Paper* 99-3560.

CASPER, K. M., BERESH, S. J. & SCHNEIDER, S. P. 2011*a* Pressure fluctuations beneath turbulent spots and instability wave packets in a hypersonic boundary layer. *AIAA Paper* 2011-0372.

CASPER, K. M., BERESH, S. J. & SCHNEIDER, S. P. 2011*b* Spanwise growth of the turbulent spot pressure-fluctuation field in a hypersonic boundary layer. *AIAA Paper* 2011-3873.

CHANG, C.-L. & CHOUDHARI, M. M. 2011 Hypersonic viscous flow over large roughness elements. *Theor. Comput. Fluid Dyn.* **25**, 85–104.

CHOUDHARI, M., LI, F., CHANG, C. L., NORRIS, A. & EDWARDS, J. 2013 Wake instabilities behind discrete roughness elements in high speed boundary layers. *AIAA Paper* 2013-0081.

CHOUDHARI, M., LI, F., WU, W., CHANG, C.-L., EDWARDS, J., KEGERISE, M. & KING, R. 2010 Laminar–turbulent transition behind discrete roughness elements in a high-speed boundary layer. *AIAA Paper* 2009-0170.

COOK, W. J. & FELDERMAN, E. J. 1966 Reduction of data from thin-film heat-transfer gauges: a concise numerical technique. *AIAA J.* **4**, 561–562.

ESTRUCH-SAMPER, D., GANAPATHISUBRAMANI, B., VANSTONE, L. & HILLIER, R. 2012 Axisymmetric flare-induced separation of high-speed transitional boundary layers. In *Proceedings of the 50th AIAA Aerospace Sciences Meeting. AIAA Paper* 2012-067.

FEDOROV, A. 2011 Transition and stability of high-speed boundary layers. *Annu. Rev. Fluid Mech.* **43**, 79–95.

FIALA, A., HILLIER, R., MALLINSON, S. G. & WIJENSINGHE, H. S. 2006 Heat transfer measurement of turbulent spots in a hypersonic blunt-body boundary layer. *J. Fluid Mech.* **555**, 81–111.

FISCHER, M. C. 1972*a* Spreading of a turbulent disturbance. *AIAA J.* **10**, 957–959.

FISCHER, M. C. 1972*b* Turbulent bursts and rings on a cone in helium at $M = 7.6$. *AIAA J.* **10**, 1387–1388.

GAD-EL-HAQ, M., BLACKWELDER, R. F. & RILEY, J. J. 1981 On the growth of turbulent regions in laminar boundary layers. *J. Fluid Mech.* **110**, 73–96.

HORVATH, T. J., BERRY, S. A., MERSKI, N. R. & FITZGERALD, S. M. 2000 X-38 experimental aerothermodynamics. *AIAA Paper* 2000-2685.

HORVATH, T. J., ZALAMEDA, J. N., WOOD, W. A., BERRY, S. A., SCHWARTZ, R. J., DANTOWITZ, R. F., SPISZ, T. S. & TAYLOR, J. C. 2012 Global infrared observations of roughness induced transition on the space shuttle Orbiter. NATO RTO-MP-AVT-200, Art. 27.

JAMES, C. S. 1958 Observation of turbulent-burst geometry and growth in supersonic flow. *NACA Tech. Rep.* 4235.

KEGERISE, M. A., KING, R., OWENS, L., CHOUDHARI, M., LI, F., CHANG, C. L. & NORRIS, A. 2012 High-speed boundary-layer transition induced by an isolated roughness element. NATO RTO-MP-AVT-200, Art. 29.

KEYES, F. G. 1952 The heat conductivity, viscosity, specific heat and Prandtl numbers for thirteen gases. *Tech. Rep.*, Massachussetts Institute of Technology, Project Squid, No. 37.

KRISHNAN, L. & SANDHAM, N. D. 2007 Strong interaction of a turbulent spot with a shock-induced separation bubble. *Phys. Fluids* **19**, 016102.

LADERMAN, A. J. 1980 Adverse pressure gradient effects on supersonic boundary-layer turbulence. *AIAA J.* **18**, 1186–1195.

MACK, L. M. 1984 Boundary layer linear stability theory. In *Special Course on Stability and Transition of Laminar Flow*. *AGARD Rep. No.* 709, vol. 3, pp. 1–81.

MALLINSON, S. G., HILLIER, R., JACKSON, A. P., KIRK, D. C., SOLTANI, S. & ZANCHETTA, M. 2000 Gun tunnel flow calibration: defining input conditions for hypersonic flow computations. *Shock Waves* **10**, 313–322.

MEE, D. J. 2001 Transition measurements on a 5° cone in the T4 shock tunnel. *Res. Rep.* No. 2001-2. University of Queensland.

MEE, D. J. 2002 Boundary-layer transition measurements in hypervelocity flows in a shock tunnel. *AIAA J.* **40**, 1542–1548.

MEE, D. J. & GOYNE, C. P. 1996 Turbulent spots in boundary layers in a free-piston shock tunnel flow. *Shock Waves* **6**, 337–343.

MORKOVIN, M. V. 1991 Panoramic view of changes in vorticity distribution on transition instabilities and turbulence. In *Boundary Layer Stability and Transition to Turbulence*, FED Series, vol. 114, pp. 1–12. ASME.

MORKOVIN, M. V., RESHOTKO, E. & HERBERT, T. 1994 Transition in open flow systems – a reassessment. *Bull. Am. Phys. Soc.* **39**, 1882.

NAGAMATSU, H. T., SHEER, R. E. & GRABER, B. C. 1967 Hypersonic laminar boundary-layer transition on 8-foot-long, 10° cone, $M_1 = 9.1$–16. *AIAA J.* **7**, 1245–1252.

REDA, D. C. 1977 Boundary-layer transition experiments on sharp, slender cones in supersonic free flight. *NSWC/NOL Tech. Rep.* No. 77-59.

REDA, D. C. 1979 Boundary-layer transition experiments on sharp, slender cones in supersonic free flight. *AIAA J.* **17**, 803–810.

REDA, D. C. 2002 Review and synthesis of roughness-dominated transition correlations for re-entry applications. *AIAA J.* **39** (2), 161–167.

REDFORD, J. A., SANDHAM, N. D. & ROBERTS, G. T. 2010 Compressibility effects on boundary-layer transition induced by an isolated roughness element. *AIAA J.* **48**, 2818–2830.

REDFORD, J. A., SANDHAM, N. D. & ROBERTS, G. T. 2012 Numerical simulations of turbulent spots in supersonic boundary layers: effects of Mach number and wall temperature. *Prog. Aerosp. Sci.* **52**, 67–79.

RESHOTKO, E. 2008 Transition issues for atmospheric re-entry. *J. Spacecr. Rockets* **45**, 161–164.

SCHNEIDER, S. P. 2004 Hypersonic laminar–turbulent transition on circular cones and scramjet forebodies. *Prog. Aerosp. Sci.* **40**, 1–50.

SCHNEIDER, S. P. 2008 Effects of roughness on hypersonic boundary-layer transition. *J. Spacecr. Rockets* **45** (2), 193–209.

SCHULTZ, D. L. & JONES, T. V. 1973; Heat-transfer measurements in short-duration hypersonic facilities. *AGARDograph* no. 165.

SOFTLEY, E. J., GRABER, B. C. & ZEMPEL, R. E. 1969 Experimental observation of transition of the hypersonic boundary layer. *AIAA J.* **7**, 257–263.

STETSON, K. F. 1988 On cone frustrum pressure gradient effects on transition. *AIAA J.* **26**, 500–502.

STETSON, K. F. & RUSHTON, G. H. 1967 Shock tunnel investigation of boundary layer transition at $M = 5.5$. *AIAA J.* **5**, 899–906.

THOMPSON, R. A. 2000 Review of X-33 hypersonic aerodynamic and aerothermodynamic development. In *Proceedings of the 22nd Congress of the International Council of the Aeronautical Sciences, Harrogate, UK*, Paper 323.

DE TULLIO, N., PAREDES, P., SANDHAM, N. D. & THEOFILIS, V. 2013 Laminar–turbulent transition induced by a discrete roughness element in a supersonic boundary layer. *J. Fluid Mech.* **735**, 613–646.

DE TULLIO, N. & SANDHAM, N. D. 2012 Direct numerical simulations of roughness receptivity and transitional shock-wave/boundary-layer interactions. NATO RTO-MP-AVT-200, pp. 1–25.

WHEATON, B. M., BARTKOWICZ, M. D., SUBBAREDDY, P. K., SCHNEIDER, S. P. & CANDLER, G. V. 2011 Roughness-induced instabilities at Mach 6: a combined numerical and experimental study. *AIAA Paper* 2011-3248.

ZANCHETTA, M. A. 1996 Kinetic heating and transition studies at hypersonic speeds. PhD thesis, University of London.

ZANCHETTA, M. A. & HILLIER, R. 1996 Blunt cone transition at hypersonic speeds: the transition reversal regime. In *Transitional Boundary Layers in Aeronautics* (ed. R. A. W. M. Henkes & J. L. van Ingen), pp. 433–440. North-Holland.